Convection–Kelvin Wave Coupling in a Global Convection-Permitting Model

NICHOLAS J. WEBER,[a] DAEHYUN KIM,[a] AND CLIFFORD F. MASS[a]

[a] *Department of Atmospheric Sciences, University of Washington, Seattle, Washington*

(Manuscript received 12 August 2020, in final form 10 December 2020)

ABSTRACT: A convectively coupled equatorial Kelvin wave (CCKW) was observed over the equatorial Indian Ocean in early November 2011 during the DYNAMO field campaign. This study examines the structure of the CCKW event using two simulations made using the MPAS model: one with 3-km grid spacing without convective parameterization and another with a 15-km grid and parameterized convection. Both simulations qualitatively capture the observed structure of the CCKW, including its vertical tilt and progression of cloud/precipitation structures. The two simulations, however, differ substantially in the amplitude of the CCKW-associated precipitation. While the 3-km run realistically captures the observed modulation of precipitation by the CCKW, the 15-km simulation severely underestimates its magnitude. To understand the difference between the two MPAS simulations regarding wave–convection coupling within the CCKW, the relationship of precipitation with convective inhibition, saturation fraction, and surface turbulent fluxes is investigated. Results show that the 15-km simulation underestimates the magnitude of the CCKW precipitation peak in association with its unrealistically linear relationship between moisture and precipitation. Precipitation, both in observations and the 3-km run, is predominantly controlled by saturation fraction and this relationship is exponential. In contrast, the parameterized convection in the 15-km run is overly sensitive to convective inhibition and not sensitive enough to environmental moisture. The implications of these results on CCKW theories are discussed.

KEYWORDS: Tropics; Convection; Kelvin waves; Cloud resolving models; Model evaluation/performance

1. Introduction

Convectively coupled Kelvin waves (CCKW) are nondispersive, eastward-propagating disturbances that contribute a significant fraction of the variability in tropical convection. CCKWs exhibit eastward propagation speeds of 10–20 m s^{-1} and zonal wavelengths of 3300–6600 km. Their vertical structure features a westward tilt of dynamical fields with height through most of the troposphere (and an eastward tilt in the upper troposphere and stratosphere), with positive temperature and specific humidity anomalies leading convection in the lower troposphere (Straub and Kiladis 2002; Roundy 2008; Kiladis et al. 2009). The typical evolution of the cloud field during CCKW passage begins with shallow convection/congestus followed by deep convective clouds spanning the full troposphere, which give way to upper-tropospheric stratiform clouds and moisture and a drier, cloud-free lower troposphere (Straub and Kiladis 2002).

CCKWs modulate the location and intensity of tropical convection and interact with a range of other tropical and extratropical phenomena. For example, the Madden–Julian oscillation (MJO; Madden and Julian 1972; Zhang 2005), a dominant mode of tropical intraseasonal variability that significantly impacts global weather on numerous various temporal and spatial scales (Zhang 2013), is often impacted by Kelvin waves (Straub et al. 2006), and vice versa (Roundy 2008). CCKWs also influence the onset of the Indian monsoon (Flatau et al. 2003) and tropical cyclogenesis (Frank and Roundy 2006; Ventrice et al. 2012).

Unfortunately, CCKWs are poorly represented in many contemporary numerical weather and climate models. For example, there is an overall lack of convectively coupled equatorial wave variance in general circulation models (GCMs), which feature unrealistically stationary convection (Dias et al. 2018). GCMs, in particular, either exhibit too little spectral power in the Kelvin wavenumber–frequency domain or simulate an unrealistic CCKW structure (e.g., Straub et al. 2010). The unsatisfactory representation of CCKWs in weather and climate models suggests the need for increased understanding of the mechanism(s) responsible for CCKW maintenance and how CCKW fidelity changes with model resolution and physics.

There have been a number of theoretical models that have produced unstable wave modes resembling observed CCKWs (e.g., Emanuel 1987; Mapes 2000, hereafter M00; Raymond and Fuchs 2007; Kuang 2008b, hereafter K08). An important application of these theoretical models is to elucidate the mechanism(s) by which coupling occurs between convection and dry Kelvin waves. The term "coupling" refers to the kinematic and thermodynamic two-way processes by which 1) a propagating dry Kelvin wave initiates, modulates, and/or maintains deep convection and 2) the convection feeds back onto the structure, magnitude, and/or propagation of the wave. While the tropical circulation response to large-scale convection (diabatic heating) is relatively well understood (Gill 1980),

Denotes content that is immediately available upon publication as open access.

Supplemental information related to this paper is available at the Journals Online website: https://doi.org/10.1175/JAS-D-20-0243.s1.

Corresponding author: Nicholas J. Weber, njweber2@atmos.washington.edu

DOI: 10.1175/JAS-D-20-0243.1

the inverse—how a propagating dynamical disturbance modifies convection—is not (Arakawa 2004). Convective parameterization, which handles wave–convection coupling in GCMs, has often been blamed for the poor CCKW simulations (Straub et al. 2010; Dias et al. 2018).

Raymond and Fuchs (2007) argued that a significant amount of tropical precipitation variability can be explained using three environmental parameters: convective inhibition, column moisture, and surface moist entropy fluxes. While recent theoretical CCKW studies have mostly emphasized the roles of convective inhibition (CIN) and column moisture in CCKW destabilization and propagation, some also suggest that surface flux feedbacks are crucial (Emanuel 2020). That is, there is still no consensus on the mechanism(s) necessary for CCKW coupling.

The ''stratiform instability'' model of M00 describes how, in radiative–convective equilibrium, large-scale waves are generated in a CIN-controlled regime when the adiabatic cooling of the lower free troposphere by a passing wave reduces CIN and excites deep convection. After a fixed period of time (3 h in the M00 model), the convection transitions to a stratiform structure that heats the upper troposphere (through condensation) and cools the lower troposphere (through evaporation), thus amplifying the initial thermal perturbation and destabilizing the wave. This model relies on boundary layer ''triggering energy'' (e.g., cold pools) for initiating convection, with shallow congestus capping wave instability through negative feedbacks (heating the lower free troposphere and increasing CIN). In the model of Raymond and Fuchs (2007), CIN variations caused by lower-tropospheric temperature anomalies are found to be critical, while radiation, surface fluxes, and column-integrated moisture are less so. This theory is supported by recent observational work that documents the correspondence of CCKW activity with CIN variations (Herman et al. 2016).

The ''moisture–stratiform instability'' theory proposed by K08 addresses the omission of moisture and unrealistic scale-independent vertical tilt in M00's stratiform instability theory. The K08 model, like in M00, decomposes the atmosphere into two vertical modes—the first and second baroclinic modes—and assumes a quasi-equilibrium between moist static energy (MSE) in the subcloud layer and saturated MSE in the lower troposphere, fostered by a near-ubiquitous shallow congestus field. Moisture–stratiform instability, unlike stratiform instability, emphasizes the role of midtropospheric moisture on the depth of convection. According to this instability mechanism, dry Kelvin waves couple to convection through the following sequence: 1) dry wave passage increases CIN with a positive lower-tropospheric thermal anomaly (allowing MSE buildup near the surface); 2) wave-scale upward motion triggers deep convection (first baroclinic mode heating), moistening the troposphere; 3) the moist troposphere allows convection to reach higher, resulting in anomalous heating (cooling) of the upper (lower) troposphere by elevated condensation (evaporation of precipitation); and 4) this heating pattern, and that associated with the shallow congestus preceding the deep convection, is in phase with the initial thermal perturbations associated with the dry wave, creating a positive feedback that destabilizes and couples the convection–dynamics system.

While these (and other) recent studies have emphasized the roles of CIN and column moisture on CCKW coupling, their relative importance is still largely unexplored. Ahmed and Neelin (2018) and Ahmed et al. (2020) recently proposed a buoyancy-based model in which these two parameters affect precipitation via lower-tropospheric plume buoyancy. Their model enables examining the relative roles of lower-tropospheric stability and moisture on precipitation within a single framework. Still, how these environmental conditions affect the timing, structure, and intensity of CCKW convection is an ongoing topic of research, one that has not been thoroughly assessed in observations or in comprehensive model simulations.

High-resolution global modeling is a valuable tool that can help improve understanding of the crucial mechanisms for CCKW maintenance and propagation, and thus provides a foundation for improving CCKW representation in GCMs. In particular, convection-permitting models (CPMs), which use horizontal grid spacing fine enough to resolve deep convective flows (≤ 4 km; e.g., Prein et al. 2015), have been shown to alleviate several biases in GCMs associated with tropical convection (Miura et al. 2007; Inoue et al. 2008; Sato et al. 2009; Stephens et al. 2010; Holloway et al. 2012; Weber and Mass 2019; Weber et al. 2020).

The bulk of previous CCKW research has only made use of observations, simplified toy/linear models, and/or coarse-resolution dynamical models with parameterized convection to investigate these waves. CPMs are excellent platforms for investigating CCKW dynamics because of their superior representation of tropical convection, which enhances the ability to identify underlying convective and coupling processes. While there have been a few studies featuring CCKWs in CPM simulations (Tomita et al. 2005; Kuang 2008a; Fuchs et al. 2014), examination of CCKW properties in a global CPM without idealization (e.g., aquaplanet, linear wave boundary conditions) is lacking in the published literature.

Recently, Weber and Mass (2019) presented results from four, month-long global CPM simulations at 3-km horizontal grid spacing, targeting cases with active convection in the Indo-Pacific warm pool. Among the convective events captured in these convection-permitting simulations was a robust CCKW that occurred during the second MJO of the Dynamics of the Madden–Julian Oscillation (DYNAMO) field campaign, which was also simulated by the same global model configuration with 15-km grid spacing and parameterized convection (Fig. 1). While a packet of organized convection propagating between 60° and roughly 100°E during the first 5 days of the forecast period is apparent in both forecast configurations and observations, the associated precipitation is considerably weaker in the 15-km simulation (M15) than in the satellite measurements (TRMM_3B42) or in the 3-km simulation (M3). The decaying propagating wave signal after ~1200 UTC 25 November 2011 in the 15-km configuration suggests that it is lacking important CCKW maintenance mechanisms that are better represented by the 3-km CPM. The contrast between two global model simulations of a CCKW offers a unique opportunity to study the mechanism(s) behind tropical wave–convection coupling.

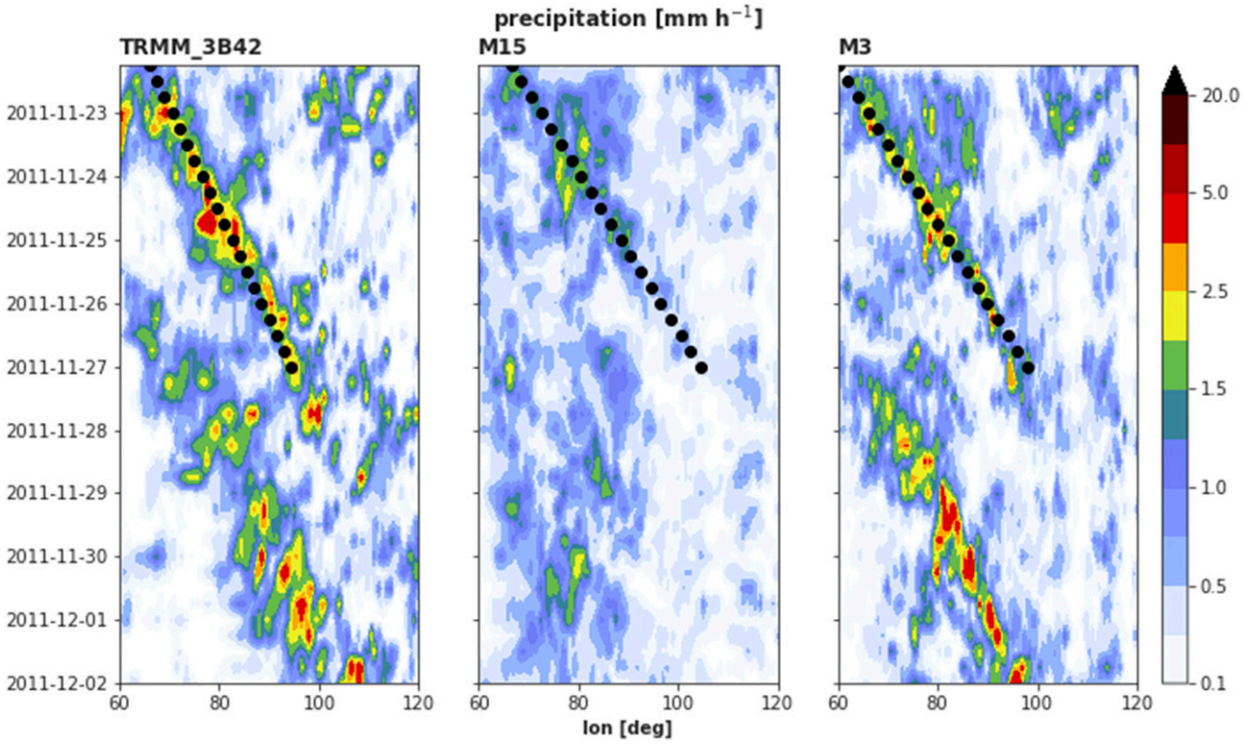

FIG. 1. Meridionally averaged (5°S to 5°N) precipitation rates from (left) TRMM satellite measurements, (center) the 15-km simulation with parameterized convection (M15), and (right) the 3-km global CPM configuration (M3). Black dots indicate tracks corresponding to the maximum integrated precipitation between 0600 UTC 22 Nov and 0000 UTC 27 Nov 2011.

Using the global model runs from Weber and Mass (2019), this study 1) examines the kinematic and thermodynamic structures of the simulated CCKW in the CPM simulation, and 2) evaluates the difference between the two model configurations (15- and 3-km simulations), with a particular focus on the wave–convection coupling. Section 2 details these model configurations, along with the verification datasets, the CCKW case details, and analysis methodology. Section 3 presents results from these simulations, which are discussed in the context of Kelvin wave coupling in section 4. Conclusions are offered in section 5.

2. Data and methods

a. Model configurations and verification data

The global simulations analyzed in this work were conducted using the Model for Prediction Across Scales (MPAS; Skamarock et al. 2012), developed at the National Center for Atmospheric Research (NCAR), and are described in more detail by Weber and Mass (2019). The model implements a horizontal C-grid centroidal Voronoi mesh (primarily composed of hexagons), which allows for smoothly transitioning variable grid spacing and improved resolution of divergent flows. Two different MPAS configurations are compared to determine the impacts of using a global CPM. The first used globally uniform 15-km horizontal grid spacing and the new Tiedtke cumulus parameterization (Zhang and Wang 2017); this configuration (hereafter M15) was designed to emulate a contemporary NWP model or high-end GCM. The second MPAS configuration, the global CPM (hereafter M3), was integrated on a uniform 3-km mesh without convective parameterization. Both meshes used 55 vertical levels and a hybrid sigma coordinate system. The integration time steps for M15 and M3 were 90 and 18 s, respectively.

Aside from the convective parameterizations, both model configurations implemented the same physics, all packaged within the MPASv5.1 "convection permitting" physics suite (described in Weber and Mass 2019). Final Operational Global Analyses from the National Centers for Environmental Prediction (NCEP) were used for atmospheric initial conditions and SST boundary conditions. SSTs were fixed at their initial values throughout the simulations.

Both MPAS simulations were integrated over 28 days for four separate cases, each featuring an MJO event in the Indo-Pacific warm pool region. Most notably, the first case, initialized at 0000 UTC 22 November 2011, captures the second MJO of the DYNAMO field campaign (Gottschalck et al. 2013). This case will be the focus of this study. MPAS forecasts are verified against Tropical Rainfall Measuring Mission (TRMM) multisatellite 3B42 satellite rainfall estimates and fifth generation European Centre for Medium-Range Weather Forecasts (ECMWF) reanalyses (ERA5). All datasets were conservatively interpolated to a regular 0.5° grid for verification. MPAS fields were linearly interpolated from the model's sigma levels onto the ERA5 pressure levels. It should be noted that the ECMWF Integrated Forecasting System (IFS) used in the ERA5 implements a version of the Tiedtke cumulus scheme similar to that used in M15.

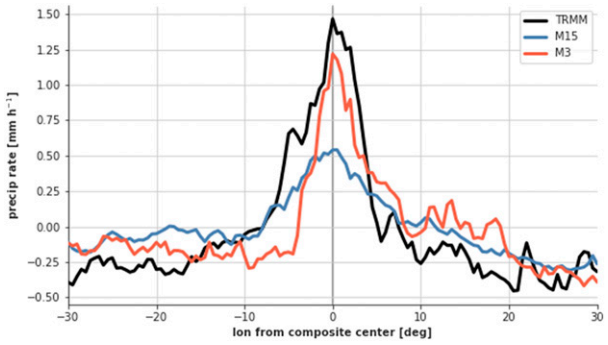

FIG. 2. Precipitation rates composited within 30° longitude of the Kelvin wave tracked in Fig. 1. Domain averages are subtracted to remove the mean state. Twenty times are included in the composite, based on 6-hourly samples over 5 days. Land grid points are excluded.

b. CCKW composite technique

The DYNAMO CCKW event is tracked from 0600 UTC 22 November to 0000 UTC 27 November 2011 by fitting lines of varying starting longitudes and phase speeds (slopes) to the meridionally averaged precipitation and selecting the track (line) with the maximum line-integrated precipitation during this period. These Kelvin wave tracks (dotted lines in Fig. 1) are used to perform composite analyses of the CCKW. The composites presented here are not sensitive to minor adjustments in the slope, starting longitude, or ending time of the composite line. This technique yields a slightly slower CCKW in TRMM ($7.7\ \mathrm{m\ s^{-1}}$) compared to in the models ($10.3\ \mathrm{m\ s^{-1}}$), though this is partially an artifact of the coarse temporal resolution.

The meridionally averaged (5°S to 5°N) precipitation rates shown in Fig. 1 are composited by longitude relative to the center of the tracked Kelvin wave, with the composite domain averages removed (Fig. 2). These and other composites are based on a sample of 20 times (5 days of 6-hourly data) using data within 30° longitude of the Kelvin wave precipitation peak. The x axes of these composites represent distance (in degrees longitude) from the convective center but can also be interpreted as time (at a single longitude) increasing toward the left, because the feature is propagating eastward. In short, the CCKW growth/development occurs to the east of the composite center, and decay to the west. The time-mean zonally averaged fields within this domain, which represent

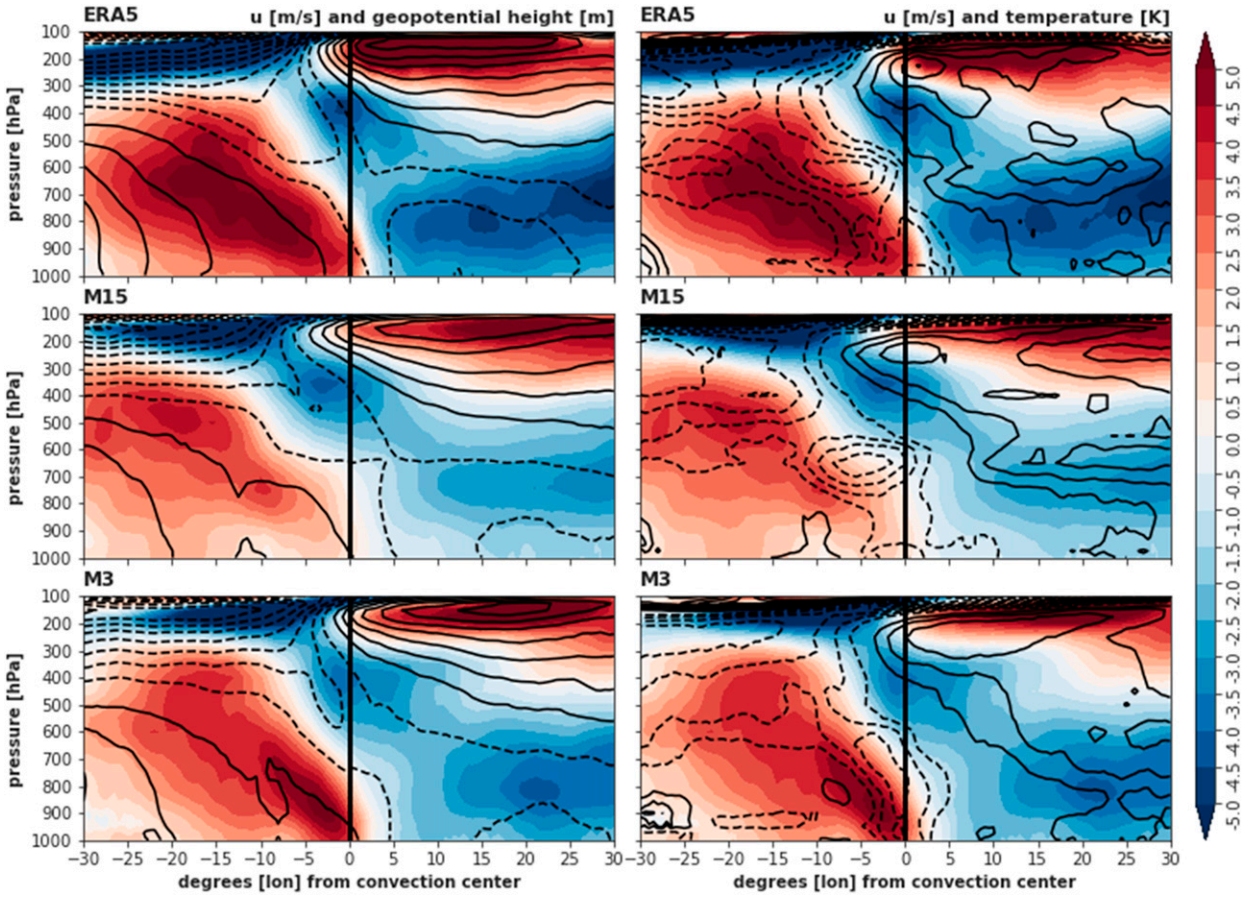

FIG. 3. Cross-section composites of zonal wind anomalies (shading) overlaid with (left) geopotential height anomalies (contours), and (right) temperature anomalies (contours). Geopotential height anomalies are contoured every 3 m between −30 and 30 m. Temperature anomalies are contoured every 0.2 K between −2 and 2 K. Solid and dashed black lines are positive and negative contours, respectively.

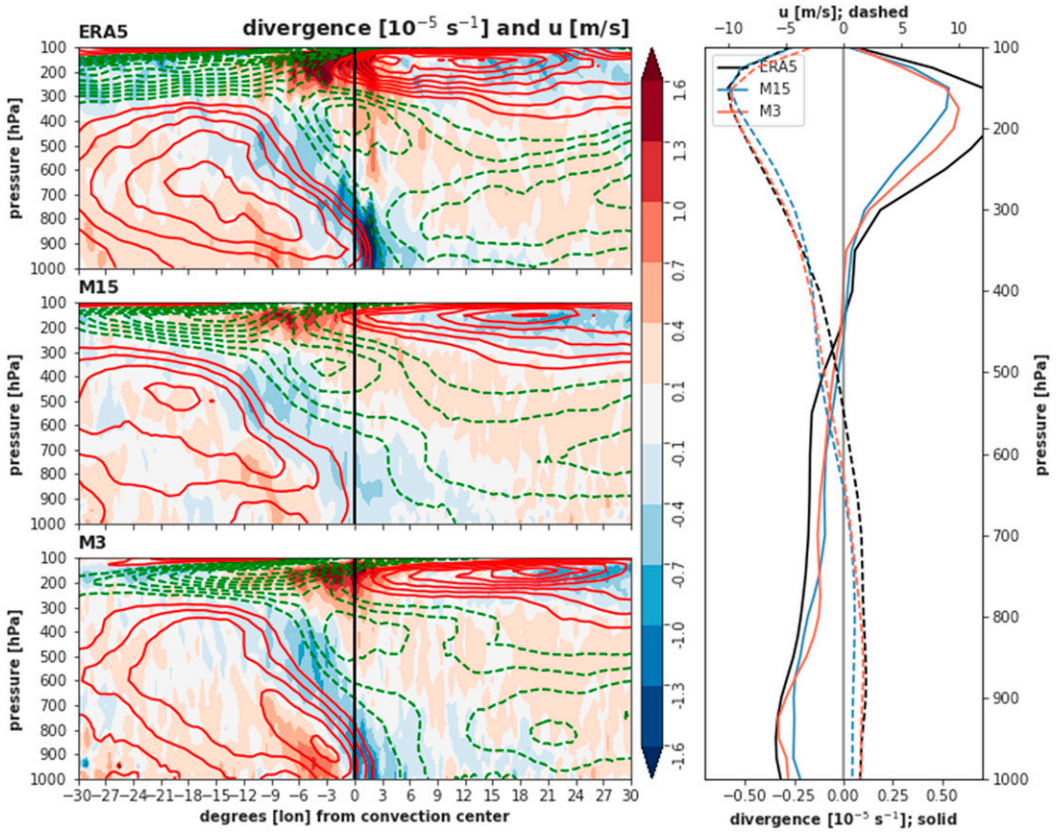

FIG. 4. (left) As in Fig. 3, but with divergence anomalies (shading) and zonal wind speed anomalies (red and green contours for positive and negative values, respectively). Zonal wind speed anomalies are contoured every 1 m s^{-1} (omitting the zero contour). (right) Average divergence (solid) and zonal wind (dashed) profiles within the composite domain (from which the anomalies were subtracted).

the large-scale environment (and partially encompass mean state biases), are removed from composites to foster intercomparison.

3. Results

a. *CCKW structure*

Before investigating the mechanisms behind the wave–convection coupling, it is important to document the evolution of the kinematic and thermodynamic structures associated with the observed and simulated CCKWs. This is done using the compositing technique described in the previous section. By design of the methodology, the precipitation peak occurs at the center of each composite (Fig. 2). As mentioned before, M15's precipitation peak is much weaker than in TRMM and M3. The composite precipitation in M3 exhibits a more realistic peak magnitude, albeit with a sharper cutoff after CCKW passage (<5° west of the composite center). The precipitation peak in M15 is broader than in M3 and TRMM, with a gentle, nearly linear, increase (decrease) during the growth (decay) phase of the CCKW.

This DYNAMO CCKW event features a fairly slow phase speed of roughly 10 m s^{-1}. While many (e.g., Kiladis et al. 2009) have attributed phase speeds of 15–20 m s^{-1} to CCKWs, others recognize a wider range, especially when the waves interact with an active MJO (Kikuchi et al. 2018). The classification of this event as a CCKW is supported by its canonical structure (Fig. 3). As in Fig. 2, fields are shown as anomalies from the composite-domain mean. The collocation of the composite zonal wind and geopotential anomalies, their near quadrature with temperature, and the westward tilt of these anomalies with height correspond well with the observed structure of CCKWs (e.g., Kiladis et al. 2009, their Fig. 8).

Figure 4 shows meridionally averaged zonal winds and horizontal divergence composited along the CCKW. The overall zonal wind structures in M15 and M3, both in the domain-mean sense (right panel) and the anomalous sense (left panels), are qualitatively similar to that of ERA5. To the west of the CCKW center, strong westerly anomalies span most of the troposphere giving way to strong easterlies above 300 hPa. East of the composite center, weak easterly anomalies span most of the troposphere capped by strong westerly anomalies in the upper troposphere. At the interface between the westerly and easterly anomalies in the lower to midtroposphere is a region of strong horizontal convergence, overlain by divergence in the upper troposphere. Consistent with previous analyses of CCKWs (e.g., Kiladis et al. 2009), the convergence exhibits a westward tilt with height. The region just east of the

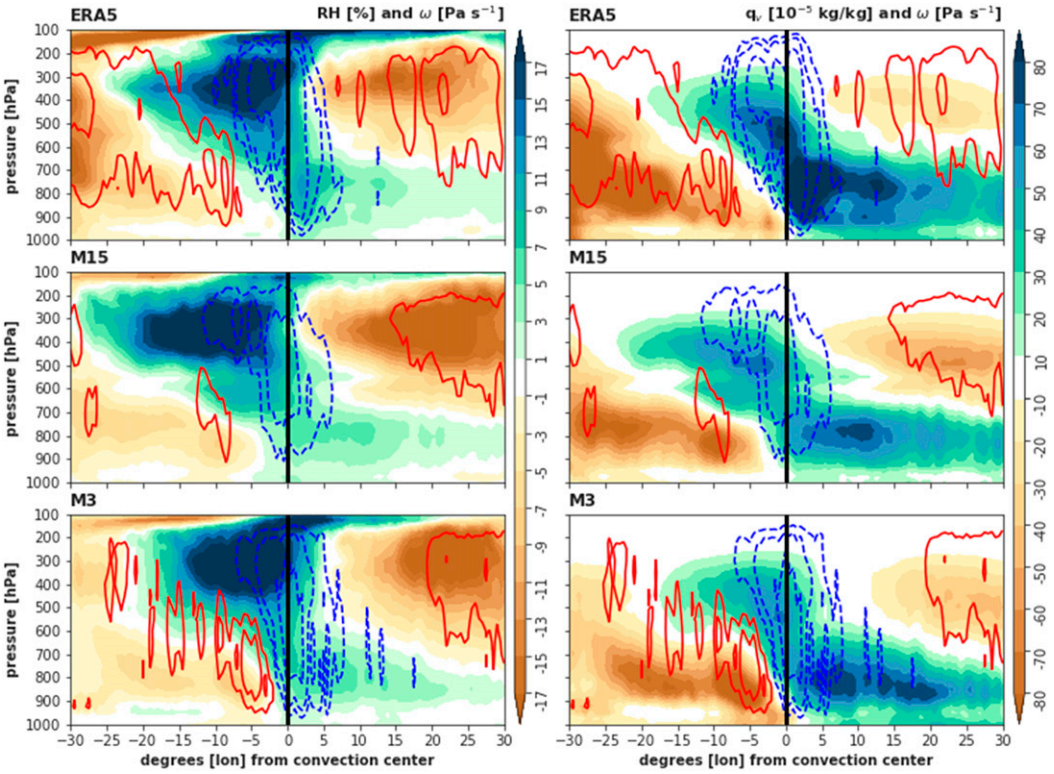

FIG. 5. As in Fig. 3, but for (left) relative humidity anomalies, and (right) specific humidity anomalies. Blue (red) contours denote pressure velocity anomalies (ω) of positive (negative) 0.05, 0.1, and 0.2 Pa s^{-1}.

composite center is characterized by near-surface convergence and upper-tropospheric divergence, indicating dominance of the first baroclinic mode. To the west, however, the composite features midlevel convergence flanked by upper- and lower-tropospheric divergence: a second baroclinic profile.

There are significant differences between M15 and M3 in Fig. 4 regarding the magnitude of the zonal flow and the divergence patterns. First, the domain-mean flow is weaker in M15 than in M3 and ERA5 (right panel). In the anomalous sense (left panels), the tropospheric westerlies to the west of the precipitation peak are much weaker in M15 than in M3 or ERA5, consistent with the weaker precipitation anomalies. The corresponding convergence in M15 is also weaker than in M3 or observations. The composite in M3 features more intense lower-tropospheric divergence to the west of the wave's convective peak, resulting in a less-tilted convergence compared to M15 and ERA5; this low-level divergence is consistent with strong downdrafts and the sharp cutoff in the M3 composite precipitation (Fig. 2).

The evolution of the CCKW moisture anomaly field, described both by relative and specific humidity, is shown in Fig. 5. Both moisture parameters reveal that the pre-CCKW environment is characterized by a moist lower troposphere and dry upper troposphere, while the post-CCKW atmosphere is dry in the lower troposphere and moist aloft. The dipole pattern in tropospheric moisture suggest a prominent second baroclinic mode structure. Only near the convective peak is the entire troposphere characterized by a single-signed (first baroclinic mode) moisture anomaly. M3 and ERA5 exhibit greater low-level moisture modulation by the CCKW than M15; ERA5, in particular, produces a strong low-level moisture maximum just east of the composite center. Implications of this evolution of the vertical moisture profile will be discussed in the context of the aforementioned CCKW theories in section 4.

To quantify the diabatic heating associated with the CCKW, apparent heat source Q_1 is calculated as the residual of the thermodynamic equation following Johnson et al. (2016), adapted from Yanai et al. (1973):

$$Q_1 \equiv \frac{\partial d}{\partial t} + \mathbf{v} \cdot \nabla d + \omega \frac{\partial d}{\partial p}, \tag{1}$$

where $d = C_{PD}T + gz$ is the dry static energy (C_{PD} is the specific heat of dry air), $\mathbf{v}$ is the horizontal wind, ω is the pressure velocity, and ∇ is the horizontal gradient operator in pressure coordinates.

Composite Q_1 is shown, along with composite vertical motion, in Fig. 6. Consistent with its weaker zonal wind and precipitation anomalies, the M15 composite exhibits weaker vertical motion and Q_1 compared to M3 and ERA5. The amplitudes of M3's upward motion and latent heat release near the convective center (Fig. 6, right panel) are much more realistic than in M15, albeit slightly weaker than in ERA5. M3's lower-tropospheric downward motion and associated evaporative cooling on the lee side of the composite center is stronger and closer to the precipitation peak, consistent with the strong near-surface divergence (Fig. 4).

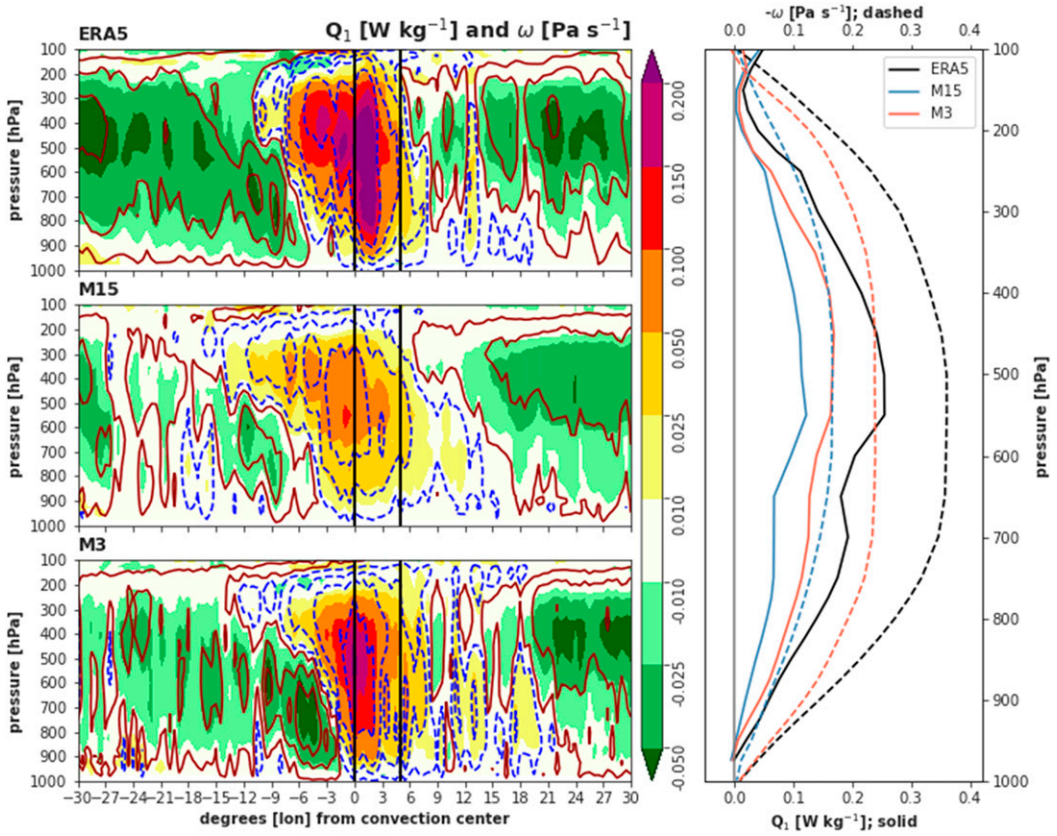

FIG. 6. (left) As in Fig. 3, but with Q_1 anomalies (shading) and ω anomalies (contours). Blue (red) contours in the cross section denote ω anomalies of positive (negative) 0.01, 0.05, 0.1, and 0.2 Pa s^{-1}. (right) Averaged profiles of the full fields within the deep convective region (0°–5° east of the center).

Figure 7 shows composites of rainwater and total cloud water, which is composed of cloud liquid, cloud ice, and snow. Snow is included because the Thompson microphysics scheme rapidly and erroneously converts cloud ice to snow (Jin et al. 2014). ERA5, M15, and M3 all feature enhanced shallow clouds (below 700 hPa) ahead of the convective center, precipitation and plentiful mid- to upper-level cloud water near the convective center, and high cloud just to the west. The cloud water and rainwater concentrations in M15, both in the anomalous sense and in the mean state, are much lower than in M3 and ERA5. Additionally, the highest concentrations of column rain and cloud water occur 6°–8° *behind* the CCKW center in M15. Only in the stratiform-dominated portion of the wave (to the west) do the two MPAS simulations produce comparable cloud and rain concentrations. In the deep convective region just east of the composite center, M15 vastly underestimates all species. The timing and concentrations of cloud and rain in M3 are consistent with both its simulated surface rain rates as in ERA5, though light rain and upper-tropospheric cloud are more widespread in M3 than in ERA5 and the anomalous stratiform clouds and precipitation in M3 subside too quickly after the wave passage.

In summary, the cross-section composites of this event suggest that the general structure of CCKWs—characterized by preceding shallow cumulus, strong deep convection and latent heating at the center, increased upper-level clouds, and a westward tilt with height (the transition between first and second baroclinic modes)—is qualitatively captured in both MPAS simulations; M3, however, exhibits a superior representation of the 3D structure of the CCKW kinematic, thermodynamic, and microphysical fields. One can hypothesize that the structural and amplitude differences noted above may be manifestations of physical processes that are poorly represented in M15: processes that may be responsible for the weaker coupling and associated convective decay (Fig. 1). This issue is explored below.

b. *Environmental drivers of CCKW precipitation*

The goal of this section is to identify the drivers of the precipitation evolution associated with the DYNAMO CCKW event. The sensitivity of the simulated (and analyzed) CCKW convection to environmental stability, moisture, and surface fluxes is investigated to see if it can account for the discrepancies in CCKW precipitation between M15 and M3.

Deep convective inhibition (DCIN), which measures environmental stability with respect to deep convection originating within the boundary layer, is adopted from Fuchs et al. (2014):

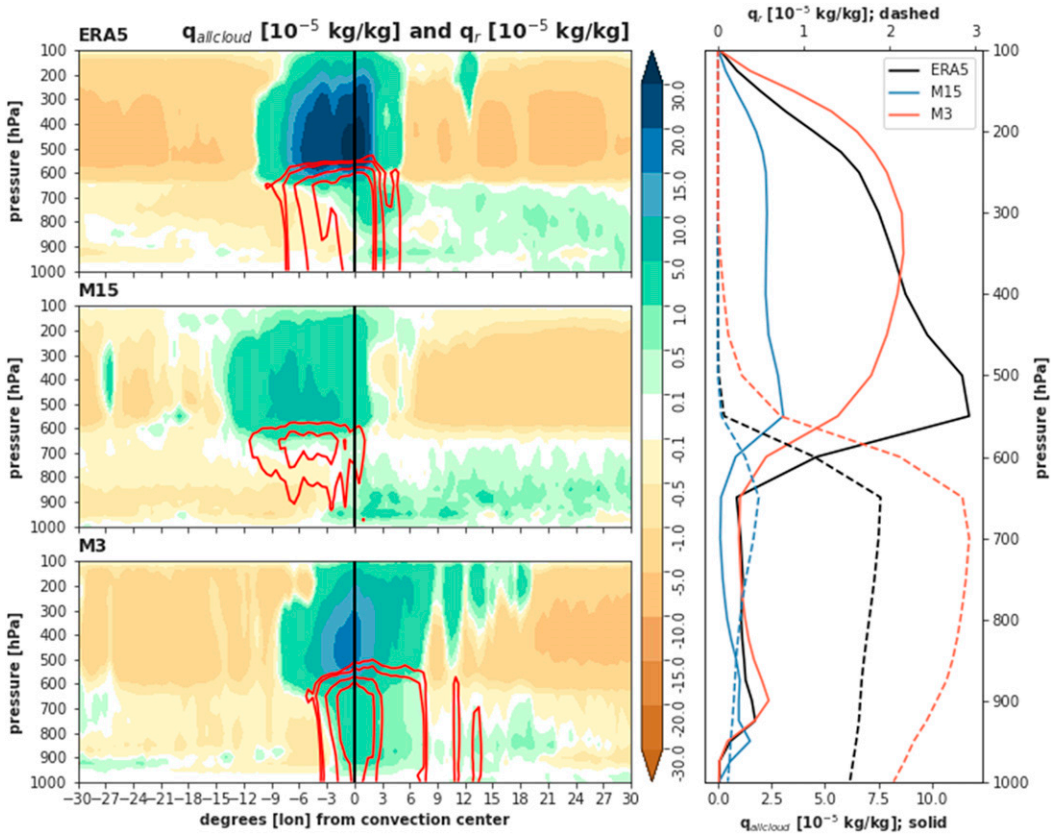

FIG. 7. As in Fig. 4, but with specific cloud water (shading) and rainwater content (red contours) anomalies. Only positive specific rainwater content anomalies are contoured (0.5, 1.0, 3.0, and 5.0 10^{-5} kg kg^{-1}).

$$\mathrm{DCIN} = s_t^* - s_{\mathrm{bl}}, \tag{2}$$

where s_t^* is the saturated moist entropy averaged just above the boundary layer, or the "threshold layer" (here, 800–750 hPa), and s_{bl} is the moist entropy averaged within the boundary layer (here, below 850 hPa). Moist entropy (and saturated moist entropy) is calculated as by Raymond (2013):

$$s = (C_{PD} + q_V C_{PV} + q_L C_{PL} + q_I C_{PI})\ln\left(\frac{T}{T_F}\right) - R_D \ln\left(\frac{p_D}{p_R}\right)$$

$$- q_V R_V \ln\left(\frac{e}{e_{SF}}\right) + \frac{L_L T_F q_V - L_F q_I}{T_F}, \tag{3}$$

where q_V, q_L, and q_I are the mixing ratios for vapor, liquid, and ice, respectively; T and p_D are temperature and pressure of dry air, respectively; e is water vapor pressure; C_{PD}, C_{PV}, C_{PL}, and C_{PI} are the respective specific heats of dry air, water vapor, liquid, and ice at constant pressure; T_F, p_R, and e_{SF} are reference values for temperature (freezing), pressure (1000 hPa), and vapor pressure (saturation value at freezing temperature), respectively; R_D and R_V are the respective gas constants for dry air and water vapor; L_L and L_F are the respective latent heats of condensation and freezing; and s_t^* and s_{bl} correspond to lower-tropospheric temperature variations and boundary layer moisture variations, respectively. The results shown below are not sensitive to the choice of pressure level bounds for the threshold layer and boundary layer.

Composites of DCIN along the Kelvin wave (Fig. 8a) reveal several interesting differences among the MPAS simulations and ERA5 dataset. All three datasets (ERA5, M15, and M3) capture the gradual decline in DCIN leading up to the composite center. This DCIN decrease is caused by the gradual erosion of s_t^* (Fig. 8b), presumably from weak, large-scale adiabatic cooling/ascent ahead of the CCKW center (Fig. 6); s_{bl} (Fig. 8c) is nearly constant during this period and thus is not contributing to the DCIN decline. Within 5°–10° east of the composite center, ERA5 and M3 experience sharp declines in DCIN caused mostly by rapidly declining s_t^* from strong adiabatic ascent. In M15, these variations in s_t^* and s_{bl} are much weaker, resulting in only a small decrease in DCIN before the convective peak. The strong convection in M3 and ERA5/TRMM rapidly depletes boundary layer moist entropy and thus forces a sharp increase in DCIN at the composite center. In other words, the deep convection following the negative DCIN anomaly in M3 and ERA5/TRMM (which is associated with stable layer, or s_t^* erosion) rapidly cools the boundary layer (with evaporating precipitation). In M15, however, the weaker convection produced slower cooling of the boundary layer, allowing the DCIN anomaly to remain negative for

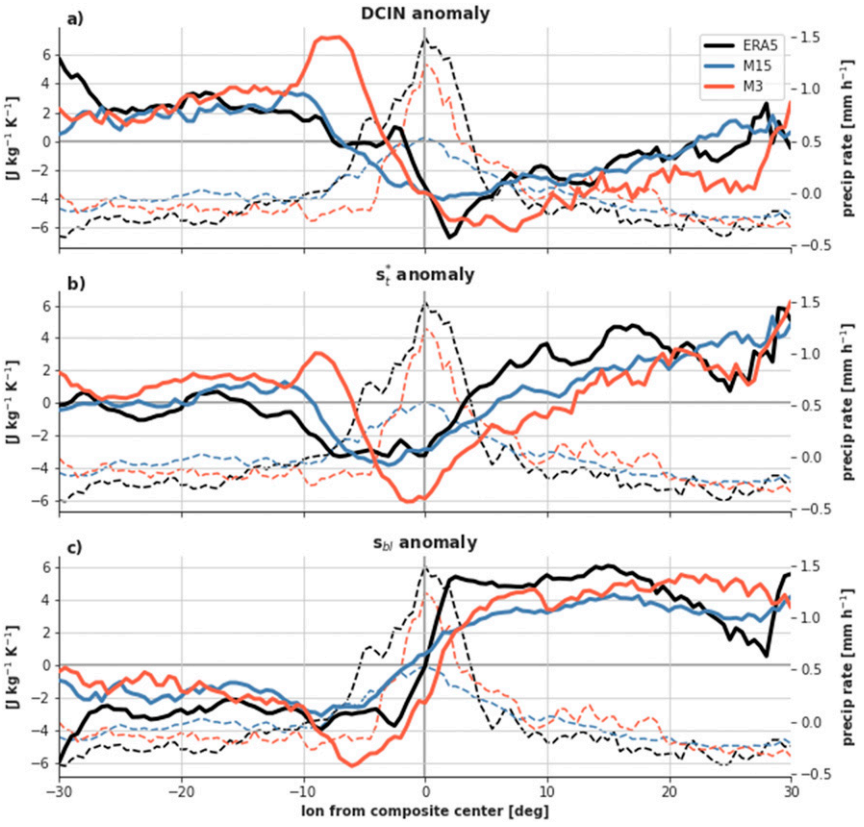

FIG. 8. As in Fig. 2, but solid lines represent composite anomalies of (a) DCIN, (b) threshold-layer saturation moist entropy s_t^* and (c) boundary layer moist entropy s_{bl}. Dashed lines are the composite precipitation anomalies from Fig. 2 (scale on the right).

longer. The occurrence of the negative peak in DCIN *before* Kelvin wave passage, along with correspondence between CCKW precipitation intensity and DCIN variability among the three datasets, corroborates previous documentation of the association between convective inhibition and CCKW onset (e.g., Fuchs et al. 2014).

Saturation fraction, which is simply the ratio of column precipitable water to saturation precipitable water (e.g., Raymond and Fuchs 2009), is composited to determine the relationship of CCKW to column moisture (Fig. 9a). For the two model simulations and the reanalysis, saturation fraction slowly increases throughout the developing phase of the CCKW (i.e., to the east of precipitation maximum) and decreases in the decaying phase, with a peak near the composite center. The saturation fraction maximum in ERA5 occurs earlier and with greater amplitude than in the MPAS simulations. M3 exhibits a strong, localized drop in saturation fraction roughly 8° west of the center. The composite saturation fraction anomaly variations in M15 are nearly identical to those in M3 leading up to the precipitation maximum. This is true for both components of the saturation fraction—precipitable water and saturation precipitable water—when composited separately (Figs. 9b,c); the increase in saturation fraction in both M15 and M3 during the CCKW growth phase is associated with an increase in column moisture (Fig. 9b) and steady tropospheric cooling (Fig. 9c). Because of its similar evolution prior to the convective peak in M15 and M3, column saturation alone cannot account for the differences in CCKW precipitation; the different responses of simulated convection to the similar moisture fluctuations, however, may be important and will be investigated later in this section.

Composite surface sensible heat and moisture flux anomalies associated with the DYNAMO CCKW are shown in Fig. 10. The CCKW-associated variations in the surface heat (Fig. 10a) and moisture (Fig. 10b) fluxes are comparable across all three datasets, with fluxes peaking slightly to the west of the composite center in association with the increase in surface wind speed (Fig. 4). Consistent with their rapid increases in near-surface westerlies, M3 and ERA5 exhibit sharper peaks in surface fluxes that coincide with the precipitation peak; the CCKW in M15, with its slower/weaker onset of low-level westerlies, experiences a more gradual increase in surface fluxes, whose peak lags the surface precipitation maximum by about 5°. In general, the concurrence or lag (i.e., in M15) of surface flux maxima relative to the CCKW convective center suggests that surface moist entropy fluxes are likely not responsible for the convective peak itself but may contribute to the maintenance of anomalous precipitation by supplying moisture.

To elucidate the coevolution of the above variables with precipitation during the DYNAMO CCKW, the composite

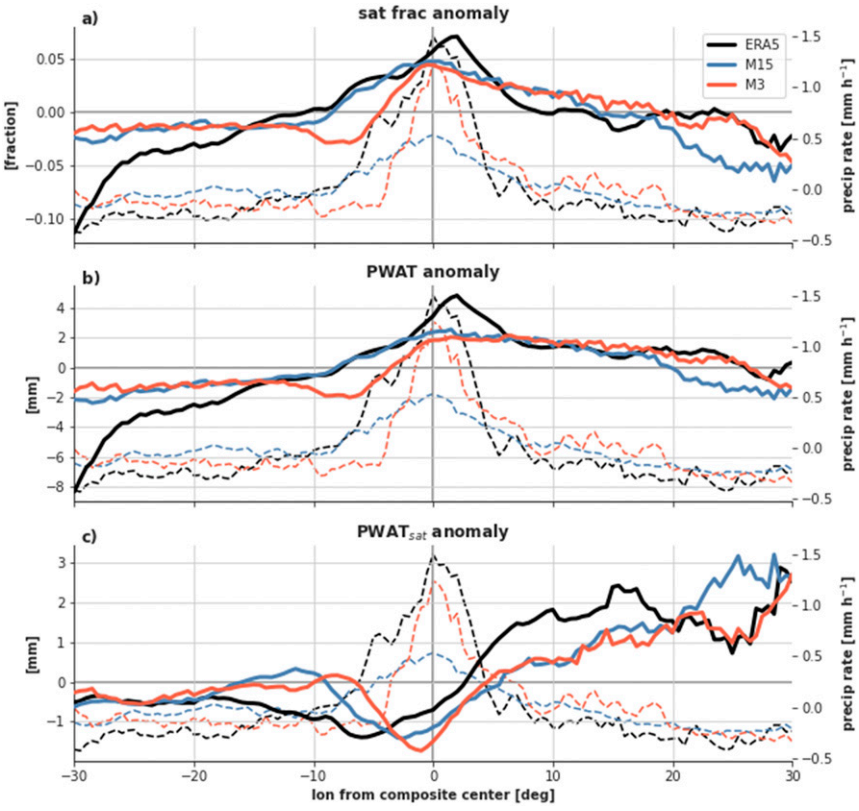

FIG. 9. As in Fig. 8, but solid lines represent composite anomalies of (a) saturation fraction, (b) precipitable water, and (c) saturation precipitable water.

values of anomalous DCIN, saturation fraction, and surface moisture flux are displayed as scatterplots versus precipitation rates (Fig. 11). The colors in these figures, delineating CCKW-relative longitude, can be interpreted as time, increasing from red to blue. Well ahead of the CCKW convection (red colors), all three datasets exhibit similar values of composite DCIN, saturation fraction, surface moisture flux, and precipitation (though the MPAS runs are a bit drier than ERA5). However, 5°–10° east of the composite center (yellow/green colors), M15 deviates substantially from M3 and ERA5. Specifically, M15 maintains a roughly linear relationship of its simulated precipitation with saturation fraction, whereas the precipitation in M3 and TRMM/ERA5 increases exponentially with rising saturation fraction. In other words, there exists a nonlinear relationship between precipitation intensity and environmental moisture/stability in observations and in M3, which appears to be largely missing in M15. Around the center of the CCKW (roughly from −5° to +5°), the simulated precipitation in all three datasets experiences a hysteresis-like behavior with respect to DCIN (i.e., different precipitation rates for a given DCIN value) and surface moisture flux, suggesting their secondary role in determining precipitation.

To determine whether the relationships in Fig. 11 are unique to this CCKW, joint distributions of DCIN, saturation fraction, and surface moisture flux versus precipitation are calculated using the full fields' values (i.e., raw model output, not anomalies) over the entire Indo-Pacific warm pool (10°S–10°N, 55°E–180°) over the entire 4-week simulation period (Fig. 12). The warm pool–averaged statistics of ERA5/TRMM and M3 both exhibit an exponential increase of precipitation rate with increasing saturation fraction, while the M15 distribution appears far more linear. The overall dependence of precipitation on DCIN is a bit more complicated, and less well represented by the evolution of the CCKW, particularly in M15. When DCIN is negative in M15, which it is for the vast majority of its precipitating grid points, the DCIN–precipitation relationship still appears roughly linear, while the relationship is less rigid in M3 and ERA5/TRMM. Warm pool precipitation in all three datasets appears to have a weaker relationship with surface moisture fluxes than with DCIN and saturation fraction. Figures 11 and 12 suggest that, among the three factors considered, precipitation over the warm pool where the DYNAMO CCKW develops is strongly modulated by saturation fraction in all datasets and by DCIN only in M15. Surface flux modulation of precipitation appears to be weak. In the following, we will focus on DCIN and saturation fraction and their modulation of precipitation.

Interpretation of precipitation's dependence on DCIN and saturation fraction is challenging because these two parameters are not mutually exclusive; they both depend on temperature and moisture. To better show how DCIN and saturation fraction modulate precipitation, the average precipitation rate

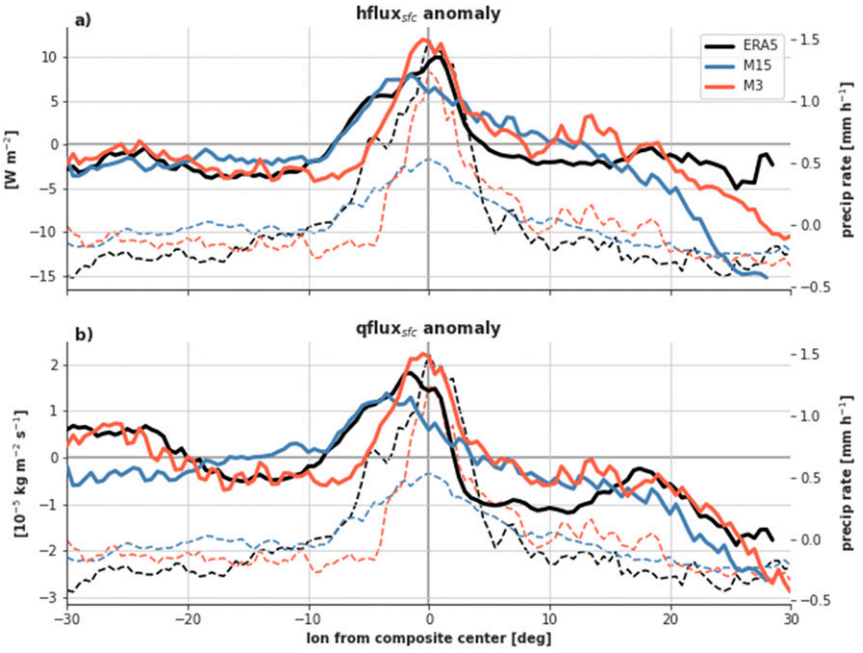

FIG. 10. As in Fig. 8, but solid lines represent composite anomalies of (a) surface heat flux and (b) surface moisture flux.

anomaly is calculated within a range of DCIN/saturation fraction anomaly bins (Fig. 13). In all three datasets it is shown that 1) DCIN and saturation fraction have an approximately linear inverse relationship with each other and 2) positive precipitation anomalies occur mainly within regions with negative DCIN and positive saturation fraction anomalies. Once those criteria are met, observed precipitation rates appear to be governed almost entirely by saturation fraction. Specifically, TRMM precipitation exhibits an exponential relationship with ERA5 saturation fraction, regardless of the DCIN value (given that it is negative). This behavior is well captured by M3, albeit with a weaker exponential precipitation rate increase for DCIN anomalies between −10 and −20 J kg^{-1} K^{-1}. M15, on the other hand, does not represent this DCIN-independent, nonlinear relationship between precipitation and saturation fraction. Rather, simulated convection in M15 is dependent on *both* DCIN and saturation fraction, and thus exhibits a weaker relationship with saturation fraction at any given DCIN value. The overdependence of M15's precipitation on DCIN—which primarily due to an unrealistic sensitivity to s_{bl} (not shown)—is likely tied to triggering criteria within the new Tiedtke cumulus scheme.

4. Discussion

Some important differences have been identified in the simulation of the CCKW in M15 versus M3. The most striking difference between M15 and M3 is the intensity of the convection—evident in the precipitation rates and latent heat release—associated with the CCKW. While CCKW composite saturation fraction evolves similarly in M15 and M3, M15 convection fails to capture the rapid increase of precipitation due the lack of nonlinearity in M15's simulated convection–moisture relationship, resulting in the weaker precipitation response of its simulated CCKW. Instead, its convection is unrealistically sensitive to changes in DCIN (Fig. 13).

The CCKW-associated precipitation in this DYNAMO case features a nearly monotonic relationship with saturation fraction, while a hysteresis-like behavior occurs with DCIN and surface fluxes (Fig. 11); the implication is that saturation fraction is the primary driver of precipitation intensity. This conclusion is also supported within the framework of Ahmed et al. (2020), in which the lower-tropospheric plume buoyancy (B_L) is represented as [their Eq. (7)]

$$B_L = g\Pi_L\left\{\frac{w_B}{\Pi_B}\frac{m_B}{m_L^*}+\frac{1}{\Pi_L}\left(\frac{w_L m_L}{m_L^*}-1\right)\right\}, \tag{4}$$

where $m = T + (L_v/c_p)q_v$ is moist enthalpy, Π is the Exner function, w is a weighting function, and g is the gravitational acceleration. For m and Π, the subscripts B and L indicate averages over the boundary layer (1000–850 hPa) and the lower-free-tropospheric layers (850–500 hPa), respectively. The values for w_B and w_L are determined following Ahmed et al. (2020). Equation (4) can be separated into two components,

$$B_L^{\mathrm{DCIN}} = g\Pi_L\left\{\frac{w_B}{\Pi_B}\frac{m_B}{em_L^*}\right\} \text{ and} \tag{5a}$$

$$B_L^{\mathrm{SF}} = g\Pi_L\left\{\frac{1}{\Pi_L}\left(\frac{w_L m_L}{m_L^*}-1\right)\right\}, \tag{5b}$$

with the former being analogous to the plume buoyancy contribution from DCIN and the latter from lower-tropospheric

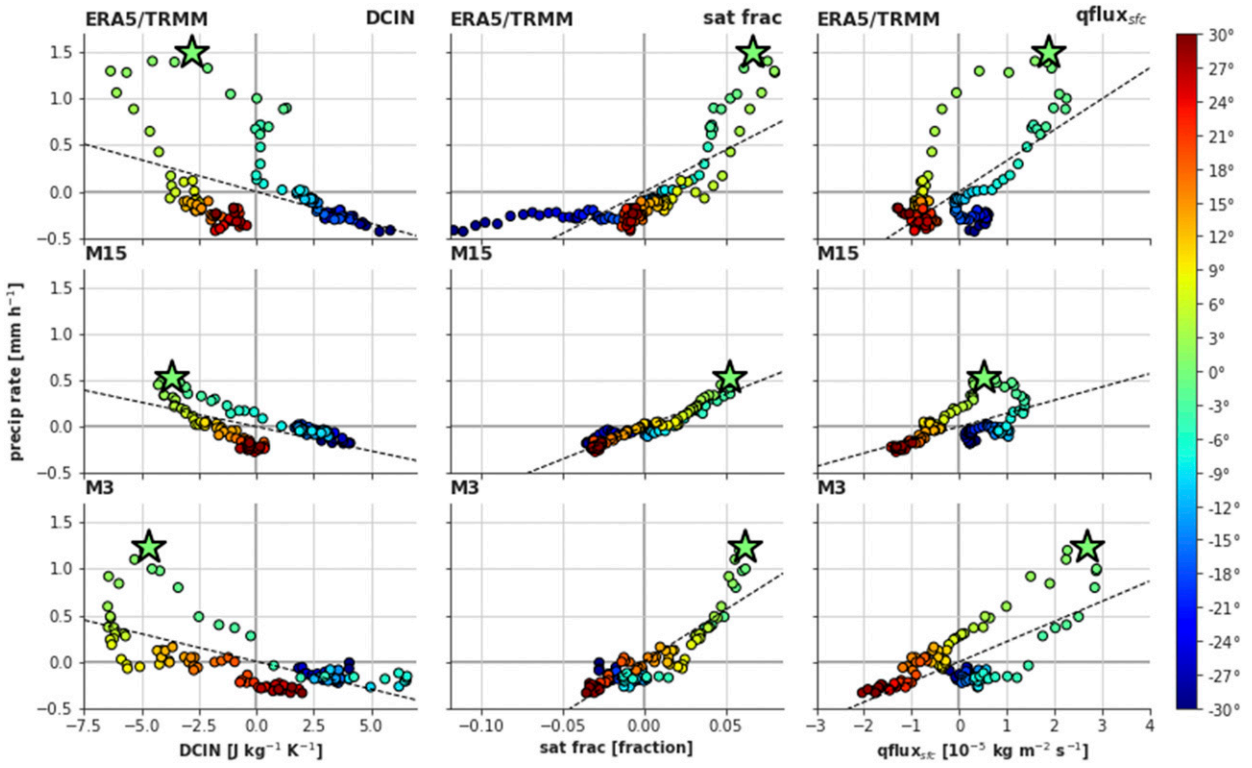

FIG. 11. Scatterplots of composite (left) DCIN, (center) saturation fraction, and (right) surface moisture flux vs composite precipitation rates. All values are anomalies from the domain mean. Colors indicate longitude from composite center (analogous to time), ranging from +30° (red) to −30° (blue). The star indicates the composite center (precipitation maximum). Black dashed lines represent linear fits, calculated by least squares regression.

saturation fraction. The evolution of precipitation in relation to these three fields throughout the CCKW life cycle (Fig. 14) indicates that precipitation in M15 is linearly dependent on both B_L^{DCIN} and B_L^{SF} as in Fig. 11. In contrast, precipitation in M3 behaves more like observed CCKW precipitation in that it increases rapidly with B_L^{SF}, while B_L^{DCIN} appears to have no control over precipitation. Also, when compared with the same unit, it is clear that the changes in B_L^{DCIN} is much weaker than that in B_L^{SF} in observations and both simulations, strongly suggesting that the increase in B_L during the developing phase of the DYNAMO CCKW is dominated by moistening in the lower troposphere.

It cannot be ruled out that surface fluxes aid in the maintenance of the convective peak by supplying column moisture and slowing the drying that occurs after the precipitation peak. However, because saturation fraction (Fig. 9a) and surface fluxes (Figs. 10a,b) evolve similarly east of the CCKW center in M15 and M3, they cannot account for the differences between the simulations. Rather, it is the convection's response to its environment—rather than the environment itself—that differentiates these two model configurations.

The new Tiedtke cumulus parameterization (Zhang and Wang 2017) used in M15 is a bulk mass flux scheme that may be unable to simulate the nonlinear precipitation–moisture relationship. A hypothesis for this deficiency is that since the scheme represents convection as isolated plumes within each grid box, the positive feedback of mesoscale convective organization—which creates larger volumes of undiluted cloudy air that enhance precipitation and associated cold pools, which then lead to further convective growth/organization—is missing within M15 (Mapes and Neale 2011). Ahn et al. (2019) showed that when the mesoscale organization of convection and its effects on plume properties are explicitly represented in a GCM (Park 2014), the GCM produced more nonlinearity in the moisture–precipitation relationship with a stronger convection at moderate–high saturation fraction. The lack of explicit representation of convective organization in M15 may also be related to the oversensitivity of its convection to DCIN variations.

Mean state biases are useful indicators of a model's ability to represent some physical processes. It is no surprise then, given its poorly simulated DCIN–moisture–precipitation relationships, that M15 exhibits significant biases in these fields (Fig. ES1 in the online supplemental material). Specifically, DCIN is much lower (by ~6 J kg^{-1} K^{-1}) in M15 than in M3 and ERA5, primarily from a cold lower-tropospheric temperature bias (not shown) that results in erroneously low s_t^* The cold troposphere in M15 also produces a slightly positive saturation fraction bias. Another contributor to the DCIN bias is a positive s_{bl} bias, which is shared by both M15 and M3. The result that M15 exhibits biases and low variability in s_b^* s_{bl}, and DCIN suggests that the unrealistically narrow convective criteria in

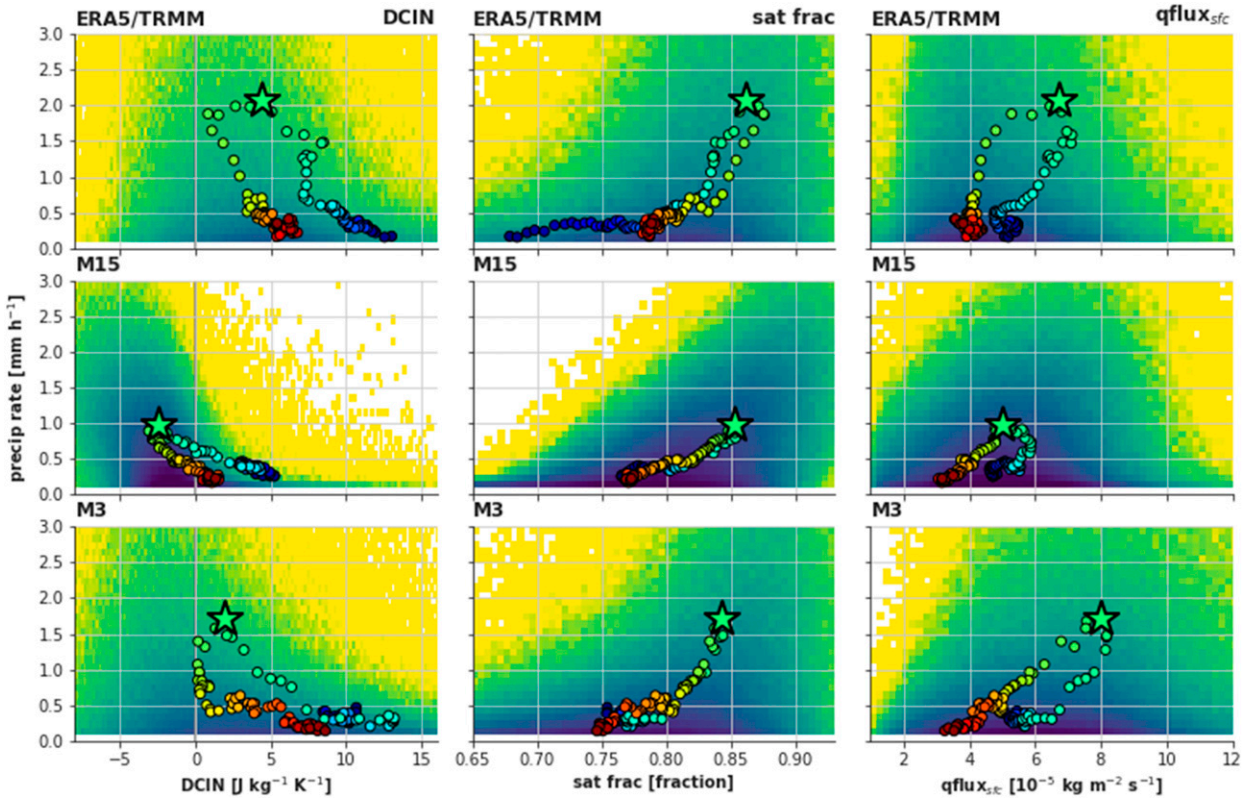

FIG. 12. As in Fig. 11, except full fields are shown instead of anomalies. Kelvin composite values (colored dots) are overlaid on 2D distributions of (left) DCIN (binned every 0.2 J kg^{-1} K^{-1}) and (center) saturation fraction (binned every 0.005), and (right) surface moisture flux (binned every 10^{-6} kg m^{-2} s^{-1}) vs precipitation rate (binned every 0.1 mm h^{-1}) over the entire Indo-Pacific warm pool and 4-week DYNAMO period. The histogram colormap is logarithmic, ranging from 10 (yellow) to 3000 (dark blue) grid points. Grid points over land are excluded from the distributions.

the Tiedtke scheme might affect the model mean state over time (as an equilibrium is reached).

Slow CCKWs such as the event examined in this study support the notion that tropical convective phenomena, rather than fitting into a binary ''gravity mode'' or ''moisture mode'' category, exist within a spectrum that ranges between the two extremes (Adames et al. 2019). This idea is also consistent with the fact that the coupling and propagation of the DYNAMO November CCKW seem to depend both on DCIN and saturation fraction, which are the primary drivers of the gravity (e.g., Herman et al. 2016) and moisture (e.g., Adames and Kim 2016) modes, respectively. While the response of convection to saturation fraction was found to be important for the strength of this CCKW, the role of DCIN in triggering the initial shallow convection and increasing saturation fraction may be crucial for the onset timing of deep convection (Fuchs et al. 2014).

Consistent with the K08 moisture–stratiform instability model, wave–convection coupling is sensitive to the strength of the moisture–precipitation relationship (i.e., the convective adjustment time scale). We conclude that the CCKW coupling in M3—evident in the stronger precipitation response (Fig. 2) and prolonged convective activity (Fig. 1)—is stronger in M3 than in M15 because of a more nonlinear moisture–precipitation relationship.

The evolution of the vertical moisture profile in this event (Fig. 5) suggests a need for reexamining the role of moisture in CCKW instability/coupling. While K08 only included mid-tropospheric (proportional to column-integrated) moisture anomalies in their model, the vertical distribution of moisture—like that of temperature and convective heating—may be important. The Kelvin wave examined here exhibits very significant variations in the second baroclinic vertical structure of moisture. Ahead of the wave, the lower troposphere is anomalously moist and the upper troposphere is dry, while the opposite is true to the west of the composite center. This moisture evolution has been noted before (e.g., Kiladis et al. 2009, their Fig. 8c), but has not been incorporated into CCKW theory. Perhaps the evolution of second baroclinic heating structures in CCKWs—rather than being a fixed-time progression of the deep convective mode (M00) or being controlled by column-integrated moisture (K08)—can be better understood by accounting for variation in the vertical structure of moisture anomalies.

5. Summary and conclusions

A convectively coupled Kelvin wave (CCKW) is simulated in two global forecast model configurations and compared

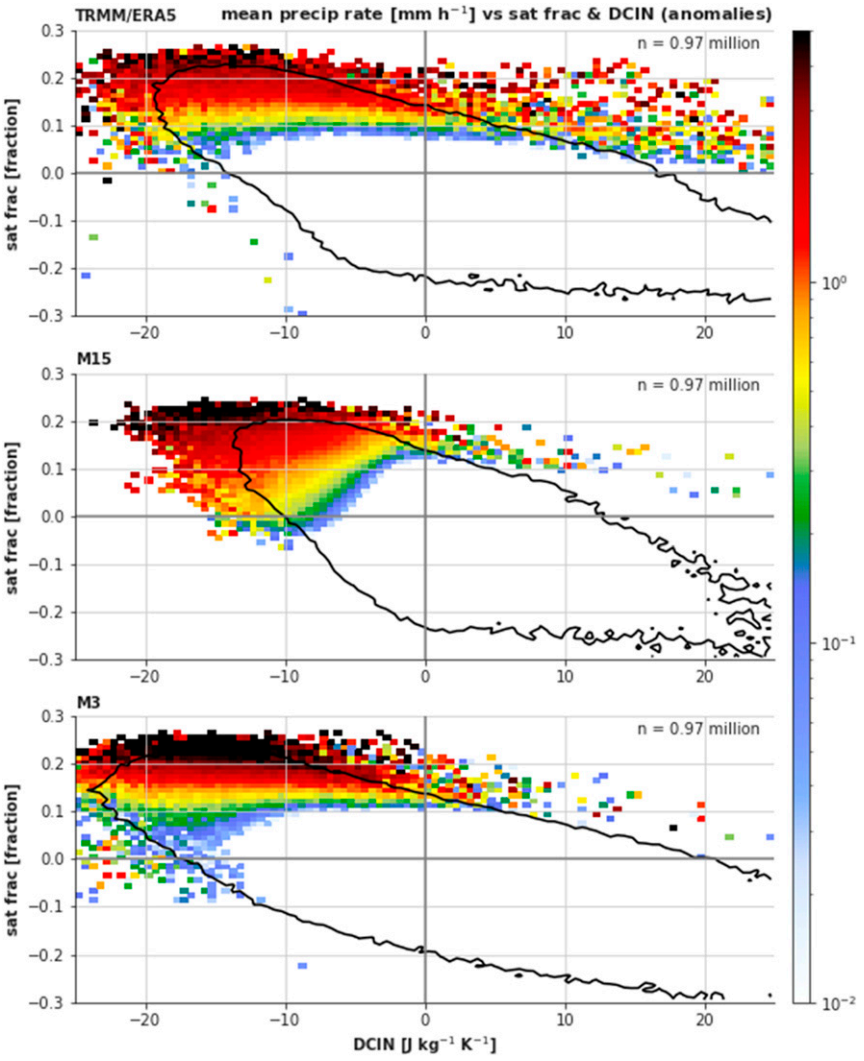

FIG. 13. Precipitation rates anomalies averaged within 2D bins of DCIN (binned every 0.5 J kg^{-1} K^{-1}) and saturation fraction (binned every 0.01). All land grid points are excluded. The color scale is logarithmic, and thus only positive anomalies are shown. The black contour indicates the region where bins contain >10 grid points.

against reanalyses and satellite precipitation estimates to identify key features of CCKW structure and elucidate coupling processes. The global 3-km convection permitting simulation (M3) captures the precipitation intensity, dynamics, microphysical species concentrations, and latent heating associated with the CCKW. The 15-km simulation with convective parameterization (M15) qualitatively captures the CCKW structure, but underestimates its overall magnitude (heating, dynamics, etc.) and cloud and rain concentrations during the convective peak and is unable to maintain the coupled wave as long as in M3 and in reanalyses.

The modulation of CCKW precipitation by deep convective inhibition (DCIN), saturation fraction, and surface turbulent fluxes is examined to understand the differences between M15 and M3. DCIN exhibits a strong minimum in M3 and ERA5 just before peak CCKW precipitation, while M15 features a much weaker fluctuation (proportional to the strength of its convection). Saturation fraction composites are nearly identical in M15 and M3 leading up to the precipitation peak; both simulations feature a steady increase in column moisture whose maximum coincides with the peak CCKW precipitation. The weaker convective response in M15 relative to M3/observations, despite exhibiting a similar moisture buildup, is attributed to an unrealistic precipitation–moisture relationship in the model. In M3 and in observations, saturation fraction is the dominant factor controlling the strength of convection, especially in moist, low-DCIN environments, and the relationship between moisture and precipitation is highly nonlinear. In M15, this relationship is more linear, and DCIN exhibits an unrealistically strong influence on precipitation intensity. While the convective response to saturation fraction is responsible for the differences between M15 and M3 in the

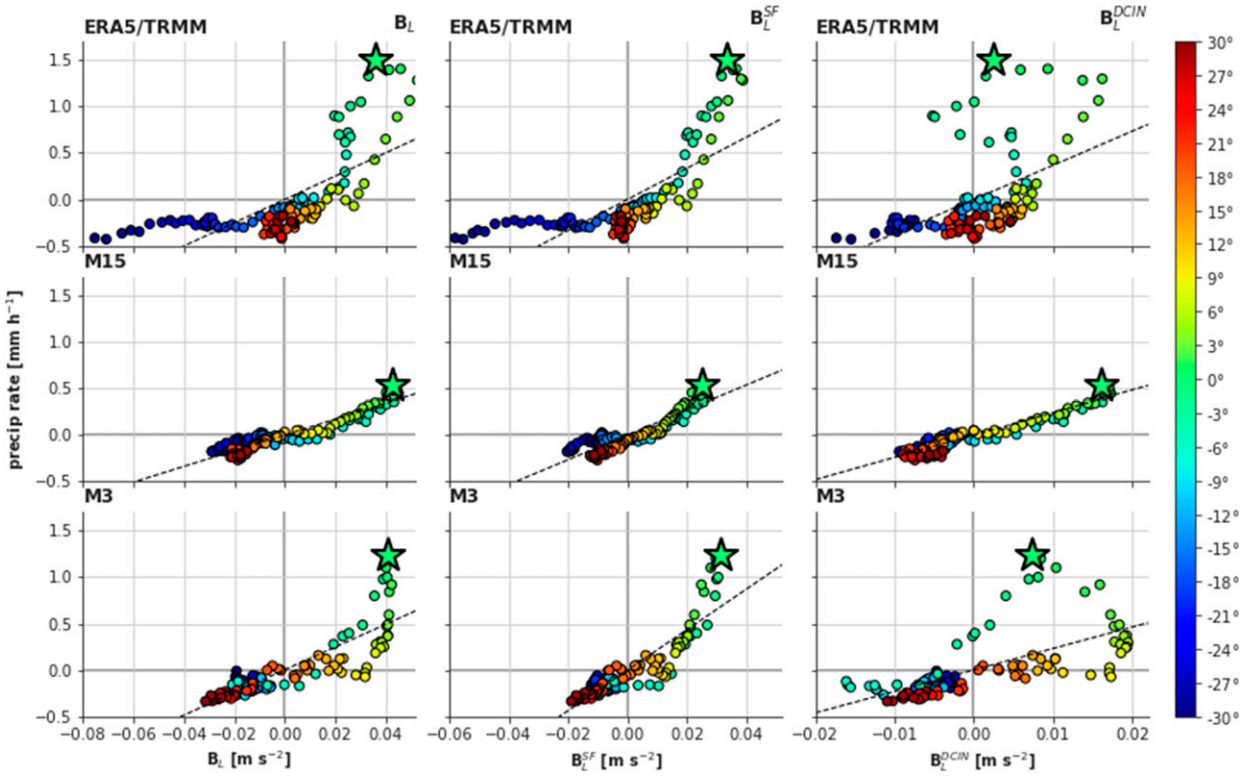

FIG. 14. As in Fig. 11, but showing composite precipitation relative to anomalous (left) B_L, (center) B_L^{SF}, and (right) B_L^{DCIN} as described in the text.

magnitude of peak rain rate associated with the CCKW, DCIN appears to be important for the initial triggering of the CCKW convection. Surface turbulent fluxes were found to only weakly affect precipitation. In summary, saturation fraction and DCIN are likely both important for wave–convection coupling: DCIN governs the timing of convective onset and moisture (specifically, the sensitivity of convection to moisture) controls the amplitude.

This work not only showcases the realism of global convection-permitting models in simulating tropical convective structures, but also demonstrates how these highly realistic simulations can be used to 1) highlight deficiencies in models with parameterized convection and 2) investigate atmospheric phenomena (like CCKWs) and the current theories describing them. While it may be years before convection-permitting models are implemented in operational forecasts (due to computational limitations), they currently represent a powerful tool for understanding convective process in both numerical simulations and the real atmosphere.

Future work in refining CCKW coupling/instability theory might involve a careful examination of the relationship between DCIN, saturation fraction, surface fluxes, and precipitation using long-term reanalyses and observational datasets. Such expanded studies may also focus on larger regions (e.g., other ocean basins) and thoroughly appraise the evolution of vertical moisture profiles with respect to CCKW latent heating.

Acknowledgments. The authors wish to thank William Skamarock, Roy Rasmussen, and Michael Duda at the National Center for Atmospheric Research (NCAR) for their support of the project and assistance with the MPAS simulations. The authors also thank Ahmed Fiaz and three anonymous reviewers for their comments on the earlier version of the manuscript. High-performance computing support on the Cheyenne supercomputer (doi:10.5065/D6RX99HX) was provided by NCAR's Computational and Information Systems Laboratory, sponsored by the National Science Foundation. NW and CM were funded by NOAA Grant NA15NWS4680023. DK was supported by NASA Grant 80NSSC17K0227, NOAA Grant NA18OAR4310300, DOE Grant DE-SC0016223, and KMA R&D Program (KMI2018-03110). The authors declare no competing interests.

Data availability statement. Global MPAS output, which is too large for a public repository, is available upon request to the authors.

REFERENCES

Adames, Á. F., and D. Kim, 2016: The MJO as a convectively coupled moisture wave: Theory and observations. *J. Atmos. Sci.*, **73**, 913–941, https://doi.org/10.1175/JAS-D-15-0170.1.

——, ——, S. K. Clark, Y. Ming, and K. Inoue, 2019: Scale analysis of moist thermodynamics in a simple model and the relationship between moisture modes and gravity waves. *J. Atmos. Sci.*, **76**, 3863–3881, https://doi.org/10.1175/JAS-D-19-0121.1.

Ahmed, F., and J. D. Neelin, 2018: Reverse engineering the tropical precipitation–buoyancy relationship. *J. Atmos. Sci.*, **75**, 1587–1608, https://doi.org/10.1175/JAS-D-17-0333.1.

——, Á. F. Adames, and J. D. Neelin, 2020: Deep convective adjustment of temperature and moisture. *J. Atmos. Sci.*, **77**, 2163–2186, https://doi.org/10.1175/JAS-D-19-0227.1.

Ahn, M.-S., D. Kim, S. Park, and Y.-G. Ham, 2019: Do we need to parameterize mesoscale convective organization to mitigate the MJO-mean state trade-off? *Geophys. Res. Lett.*, **46**, 2293–2301, https://doi.org/10.1029/2018GL080314.

Arakawa, A., 2004: The cumulus parameterization problem: Past, present, and future. *J. Climate*, **17**, 2493–2525, https://doi.org/10.1175/1520-0442(2004)017<2493:RATCPP>2.0.CO;2.

Charney, J. G., and A. Eliassen, 1964: On the growth of the hurricane depression. *J. Atmos. Sci.*, **21**, 68–75, https://doi.org/10.1175/1520-0469(1964)021<0068:OTGOTH>2.0.CO;2.

Dias, J., M. Gehne, G. N. Kiladis, N. Sakaeda, P. Bechtold, and T. Haiden, 2018: Equatorial waves and the skill of NCEP and ECMWF numerical weather prediction systems. *Mon. Wea. Rev.*, **146**, 1763–1784, https://doi.org/10.1175/MWR-D-17-0362.1.

Emanuel, K. A., 1987: An air–sea interaction model of intraseasonal oscillations in the tropics. *J. Atmos. Sci.*, **44**, 2324–2340, https://doi.org/10.1175/1520-0469(1987)044<2324:AASIMO>2.0.CO;2.

——, 2020: Slow modes of the equatorial waveguide. *J. Atmos. Sci.*, **77**, 1575–1582, https://doi.org/10.1175/JAS-D-19-0281.1.

Flatau, M. K., P. J. Flatau, J. Schmidt, and G. N. Kiladis, 2003: Delayed onset of the 2002 Indian monsoon. *Geophys. Res. Lett.*, **30**, 1768, https://doi.org/10.1029/2003GL017434.

Frank, W. M., and P. E. Roundy, 2006: The role of tropical waves in tropical cyclogenesis. *Mon. Wea. Rev.*, **134**, 2397–2417, https://doi.org/10.1175/MWR3204.1.

Fuchs, Ž., S. L. Sessions, and D. J. Raymond, 2014: Mechanisms controlling the onset of simulated convectively coupled Kelvin waves. *Tellus*, **66A**, 22107, https://doi.org/10.3402/tellusa.v66.22107.

Gill, A. E., 1980: Some simple solutions for heat-induced tropical circulation. *Quart. J. Roy. Meteor. Soc.*, **106**, 447–462, https://doi.org/10.1002/qj.49710644905.

Gottschalck, J., P. E. Roundy, C. J. Schreck III, A. Vintzileos, and C. Zhang, 2013: Large-scale atmospheric and oceanic conditions during the 2011–12 DYNAMO field campaign. *Mon. Wea. Rev.*, **141**, 4173–4196, https://doi.org/10.1175/MWR-D-13-00022.1.

Hannah, W. M., and E. D. Maloney, 2014: The moist static energy budget in NCAR CAM5 hindcasts during DYNAMO. *J. Adv. Model. Earth Syst.*, **6**, 420–440, https://doi.org/10.1002/2013MS000272.

Herman, M. J., Z. Fuchs, D. J. Raymond, and P. Bechtold, 2016: Convectively coupled Kelvin waves: From linear theory to global models. *J. Atmos. Sci.*, **73**, 407–428, https://doi.org/10.1175/JAS-D-15-0153.1.

Holloway, C. E., S. J. Woolnough, and G. M. S. Lister, 2012: Precipitation distributions for explicit versus parametrized convection in a large-domain high-resolution tropical case study. *Quart. J. Roy. Meteor. Soc.*, **138**, 1692–1708, https://doi.org/10.1002/qj.1903.

Inoue, R., M. Satoh, H. Miura, and B. Mapes, 2008: Characteristics of cloud size of deep convection simulated by a global cloud resolving model over the western tropical Pacific. *J. Meteor. Soc. Japan*, **86A**, 1–15, https://doi.org/10.2151/jmsj.86A.1.

Jin, Y., and Coauthors, 2014: The impact of ice phase cloud parameterizations on tropical cyclone prediction. *Mon. Wea. Rev.*, **142**, 606–625, https://doi.org/10.1175/MWR-D-13-00058.1.

Johnson, R. H., P. E. Ciesielski, and T. M. Rickenbach, 2016: A further look at Q1 and Q2 from TOGA COARE. *Multiscale Convection-Coupled Systems in the Tropics: A Tribute to Dr. Michio Yanai*, *Meteor. Monogr.*, No. 56, Amer. Meteor. Soc., https://doi.org/10.1175/AMSMONOGRAPHS-D-15-0002.1.

Kikuchi, K., G. N. Kiladis, J. Dias, and T. Nasuno, 2018: Convectively coupled equatorial waves within the MJO during CINDY/DYNAMO: Slow Kelvin waves as building blocks. *Climate Dyn.*, **50**, 4211–4230, https://doi.org/10.1007/s00382-017-3869-5.

Kiladis, G. N., M. Wheeler, P. T. Haertel, K. H. Straub, and P. E. Roundy, 2009: Convectively coupled equatorial waves. *Rev. Geophys.*, **47**, RG2003, https://doi.org/10.1029/2008RG000266.

Kuang, Z., 2008a: Modeling the interaction between cumulus convection and linear gravity waves using a limited-domain cloud system–resolving model. *J. Atmos. Sci.*, **65**, 576–591, https://doi.org/10.1175/2007JAS2399.1.

——, 2008b: A moisture-stratiform instability for convectively coupled waves. *J. Atmos. Sci.*, **65**, 834–854, https://doi.org/10.1175/2007JAS2444.1.

Madden, R. A., and P. R. Julian, 1972: Description of global-scale circulation cells in the tropics with a 40–50 day period. *J. Atmos. Sci.*, **29**, 1109–1123, https://doi.org/10.1175/1520-0469(1972)029<1109:DOGSCC>2.0.CO;2.

Mapes, B., 2000: Convective inhibition, subgrid-scale triggering energy, and stratiform instability in a toy tropical wave model. *J. Atmos. Sci.*, **57**, 1515–1535, https://doi.org/10.1175/1520-0469(2000)057<1515:CISSTE>2.0.CO;2.

——, and R. Neale, 2011: Parameterizing convective organization to escape the entrainment dilemma. *J. Adv. Model. Earth Syst.*, **3**, M06004, https://doi.org/10.1029/2011MS000042.

Miura, H., M. Satoh, T. Nasuno, A. T. Noda, and K. Oouchi, 2007: A Madden–Julian oscillation event realistically simulated by a global cloud-resolving model. *Science*, **318**, 1763–1765, https://doi.org/10.1126/science.1148443.

Park, S., 2014: A unified convection scheme (UNICON). Part I: Formulation. *J. Atmos. Sci.*, **71**, 3902–3930, https://doi.org/10.1175/JAS-D-13-0233.1.

Prein, A. F., and Coauthors, 2015: A review on regional convection-permitting climate modeling: Demonstrations, prospects, and challenges. *Rev. Geophys.*, **53**, 323–361, https://doi.org/10.1002/2014RG000475.

Raymond, D. J., 2013: Sources and sinks of entropy in the atmosphere. *J. Adv. Model. Earth Syst.*, **5**, 755–763, https://doi.org/10.1002/jame.20050.

——, and Ž. Fuchs, 2007: Convectively coupled gravity and moisture modes in a simple atmospheric model. *Tellus*, **59**, 627–640, https://doi.org/10.1111/j.1600-0870.2007.00268.x.

——, and ——, 2009: Moisture modes and the Madden–Julian oscillation. *J. Climate*, **22**, 3031–3046, https://doi.org/10.1175/2008JCLI2739.1.

Roundy, P. E., 2008: Analysis of convectively coupled Kelvin waves in the Indian Ocean MJO. *J. Atmos. Sci.*, **65**, 1342–1359, https://doi.org/10.1175/2007JAS2345.1.

Sato, T., H. Miura, M. Satoh, Y. N. Takayabu, and Y. Wang, 2009: Diurnal cycle of precipitation in the tropics simulated in a global cloud-resolving model. *J. Climate*, **22**, 4809–4826, https://doi.org/10.1175/2009JCLI2890.1.

Skamarock, W. C., J. B. Klemp, M. G. Duda, L. D. Fowler, S.-H. Park, and T. D. Ringler, 2012: A multiscale nonhydrostatic atmospheric model using centroidal Voronoi tessellations and C-grid staggering. *Mon. Wea. Rev.*, **140**, 3090–3105, https://doi.org/10.1175/MWR-D-11-00215.1.

Stephens, G., and Coauthors, 2010: Dreary state of precipitation in global models. *J. Geophys. Res.*, **115**, D24211, https://doi.org/10.1029/2010JD014532.

Straub, K. H., and G. N. Kiladis, 2002: Observations of a convectively coupled Kelvin wave in the eastern Pacific ITCZ. *J. Atmos. Sci.*, **59**, 30–53, https://doi.org/10.1175/1520-0469(2002)059<0030:OOACCK>2.0.CO;2.

——, ——, and P. E. Ciesielski, 2006: The role of equatorial waves in the onset of the South China Sea summer monsoon and the demise of El Niño during 1998. *Dyn. Atmos. Oceans*, **42**, 216–238, https://doi.org/10.1016/j.dynatmoce.2006.02.005.

——, P. T. Haertel, and G. N. Kiladis, 2010: An analysis of convectively coupled Kelvin waves in 20 WCRP CMIP3 global coupled climate models. *J. Climate*, **23**, 3031–3056, https://doi.org/10.1175/2009JCLI3422.1.

Tomita, H., H. Miura, S. Iga, T. Nasuno, and M. Satoh, 2005: A global cloud-resolving simulation: Preliminary results from an aqua planet experiment. *Geophys. Res. Lett.*, **32**, L08805, https://doi.org/10.1029/2005GL022459.

Ventrice, M. J., C. D. Thorncroft, and C. J. Schreck III, 2012: Impacts of convectively coupled Kelvin waves on environmental conditions for Atlantic tropical cyclogenesis. *Mon. Wea. Rev.*, **140**, 2198–2214, https://doi.org/10.1175/MWR-D-11-00305.1.

Weber, N. J., and C. F. Mass, 2019: Subseasonal weather prediction in a global convection-permitting model. *Bull. Amer. Meteor. Soc.*, **100**, 1079–1089, https://doi.org/10.1175/BAMS-D-18-0210.1.

——, ——, and D. Kim, 2020: The impacts of horizontal grid spacing and cumulus parameterization on subseasonal prediction in a global convection-permitting model. *Mon. Wea. Rev.*, **148**, 4747–4765, https://doi.org/10.1175/MWR-D-20-0171.1.

Yanai, M., S. Esbensen, and J.-H. Chu, 1973: Determination of bulk properties of tropical cloud clusters from large-scale heat and moisture budgets. *J. Atmos. Sci.*, **30**, 611–627, https://doi.org/10.1175/1520-0469(1973)030<0611:DOBPOT>2.0.CO;2.

Zhang, C., 2005: Madden–Julian oscillation. *Rev. Geophys.*, **43**, RG2003, https://doi.org/10.1029/2004RG000158.

——, 2013: Madden–Julian oscillation: Bridging weather and climate. *Bull. Amer. Meteor. Soc.*, **94**, 1849–1870, https://doi.org/10.1175/BAMS-D-12-00026.1.

——, and Y. Wang, 2017: Projected future changes of tropical cyclone activity over the western North and South Pacific in a 20-km-mesh regional climate model. *J. Climate*, **30**, 5923–5941, https://doi.org/10.1175/JCLI-D-16-0597.1.